Design and Optimization of Quadrilateral Shaped PVDF Cantilever for Efficient Conversion of Energy from Ambient Vibration

Babak Montazer, and Utpal Sarma, *Member, IEEE*

Abstract—**This paper addresses an efficient way of conversion of ambient vibrational energy to electrical by structure optimization of piezoelectric film. Polyvinylidene fluoride (PVDF) has been used for this study. The effects of shape variations of cantilever beam with multilayer configuration based on Euler–Bernoulli theorem without considering the proof mass attached at the free end has been investigated in this work. Most of piezoelectric vibrational energy harvesters (PVEHs) are designed considering the presence of proof mass and in this work it has been tried to convey the idea, that with the new optimized shape, the cantilever itself can behave as a flexible proof mass for energy enhancement. The possibility of harvesting energy from three different geometries: a) Near Edge Width Quadratic (NEWQ), b) Half Quadratic (HQ) and c) Trapezoidal has been presented. Scanning Electron Microscopy is used to measure the thickness of the various layers. The NEWQ design shows the best performance in terms of power and resonance frequency ($f_r < 200Hz$) compared to the others.Here, the study of the piezo-film models using finite element method (FEM) simulation software (COMSOL Multiphysics optimization module) and experimental validation are also presented. Using the models, the generation of voltage/power has been analyzed under various excitation frequency and load resistance. Moreover, stress/strain distribution and the displacement have also been highlighted in this study.**

Index Terms—**Energy harvester, multilayer cantilever, PVDF film, ambient vibrational energy.**

I. INTRODUCTION

Portableland wearable self-powered devices have been of great interest for powering wireless sensor nodes, mobile systems and health monitoring systems. Ambient vibration is a huge free energy source which is unused and wasted in the environment, e.g. vibrations caused by industrial machines, vehicles and engines. Research and development for efficient energy harvester from mechanical vibration (electrostatic, electromagnetic and piezoelectric) have seen accelerated growth in the recent years. In such study piezopolymers are widely used due to its advantages like lower cost, easier process of fabrication and capability to increase deformation of the material [1, 2] .

Various studies have been carried out on piezopolymer to find out more information about the characteristics of the piezoelectric material [3–5] .The PVDF piezo film is usually used in sensors and actuators. This is because of β phase of the crystal has a strong dipole moment, which has the ability to convert mechanical deformation into electrical energy and vice versa [6]. Human foot pressure is a source to harvest energy by the use of PVDF and PZT material which are placed in the insole of shoes [7]. Vatansever *et al.*[8] in a study proposed different piezoelectric films and studied mechanical stimulus of PVDF in vacuum at different temperatures under damped vibration. The results of the study showed that the longer sample produces lower voltage for an extended period, but the shorter sample generates higher voltage in shorter time. Moreover, this study reveals that the influence of vacuum is more than the temperature variation on generated voltage.

Optimization and implementation of shape of piezoelectric cantilevers have been reported by several researchers, such as rectangular [9] and [10] or trapezoidal shapes [11]. An optimized array of piezoelectric patch with rectangular shape on a square shaped substrate has been analyzed [12]. In the same line, an array of individual beams by using separate set of piezoelectric patch has been investigated and reported [13]. The performance of two arc-shaped piezoelectric cantilevers, polarized in a radial curve direction, has been reported and the energy generated is found to be 2.55-4.24 times higher than a plane cantilever [14]. However, the effective volume occupied by the prototype is high. Different shapes of cantilevers have been designed and optimized by using PVDF material and excited by a rotary movement. It reveals that the optimal straight sided with a curved shape have better performance as compared with tapered cantilever [15]. In another work, researchers have investigated the model of linear and quadratic shapes with attached proof mass at the free end of the beam. They found that the resonance frequency is less and power generation is higher in the quadratic shaped cantilever. This work also establishes that the quadratic shaped cantilever is capable to generate energy two times more than a rectangular

The authors with the Department of Instrumentation & USIC, Gauhati University, Guwahati, 781014, India (e-mail: babakmont1212@gmail.com; utpal.sarma.in@ieee.org).

one [16]. An analytical model of exponential tapering shape of the piezoelectric unimorph and bimorph cantilever has been presented and performance of bimorph cantilever under series and parallel connections has been analyzed [17]. Lee *et al*.[18]designed rectangular and trapezoidal cantilevers to compare their performances. They concluded that trapezoidal shaped cantilever generates more energy than the rectangular shaped one as it has additional strained region. In a similar study, optimization of rectangular and triangular shaped cantilever were carried out, as a result it was found that, power enhancement in triangular shape can be obtained at a particular length-to-width ratio with a constant resonance frequency[19]. Friswell *et al* .[20] tried to increase power in piezoelectric sensor by determining the effect of width and slope using finite element method (FEM) simulation. Analysis of capacitance of piezoelectric layer and coupling factor revealed the simultaneous effect of power enhancement. Thein *et al*.[21] analyzed the output power using FEM simulation and have shown that power density increases in bimorph cantilever with optimized shape of the cantilever with holes.

This paper presents the analysis, optimization and implementation of PVDF specimens for three different shapes: Near edge width quadratic (NEWQ), Half quadratic (HQ) and Trapezoidal. The end of each cantilever is supported by a customised vibrator to provide sinusoidal vibration. The focus of this work is to optimize the shape of the PVDF specimens and obtain high power generation through coupling the load resistance. The strain profile of the non-symmetric cantilever with different shapes has been simulated using the FEM. The volume of two quadratic models are almost equal and the NEWQ model generates maximum energy at lowest resonance frequency due to higher strain distribution over the cantilever beam. In addition, the performance of the harvesters in terms of generated voltage/power at different frequencies are investigated. These three samples are compared with other traditional sample (rectangular) using simulation and same experimental setup. Finally, the comparison between optimum and conventional configurations (with and without proof mass) is discussed in this paper.

II. Sample Characterization

The multilayer stack of piezoelectric film LDT0-028 K/L from Measurement Specialties has been considered for this study. The piezoelectric film PVDF is sandwiched between two Ag (silver) electrodes, where a polyester (PET) layer laminates is at the bottom of the electrode and a very thin layer of acrylic laminate is on the top of the cantilever as shown in Fig. 1. The cross-section of the multilayer piezoelectric film has been characterized by energy dispersive spectroscopy (EDS) and presence of all main elements (Ag, F, O, and C) have been found (Fig. 1(a)). In addition, the approximate thickness of each layer has been estimated using Field Emission Scanning Electron Microscope (FESEM) image as depicted in Fig. 1(b). For this study three different shapes, I: Near edge width quadratic (NEWQ), II: Half quadratic in middle (HQ) and III: trapezoidal has been prepared. Table I shows the dimensions of the samples after cutting out from main original sample

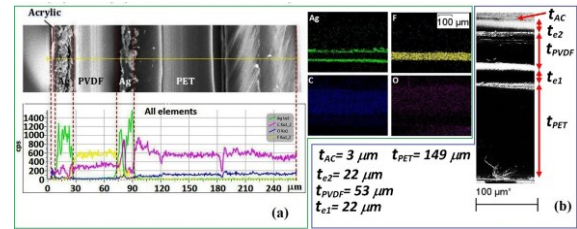(rectangular). All dimensions are labeled in accordance with the

Fig. 1. The multilayer harvester (a) Cross sectional view of the sample, characterized by energy dispersive spectroscopy (EDS) and (b) Thickness measured by use of FESEM.

Fig .2(a), (b) and (c) and also include active layers Fig .2 (d) and (e). The width of the film is varied, keeping the length and the thickness at almost constant value. The electrical and the mechanical properties of the material are listed in Table II.
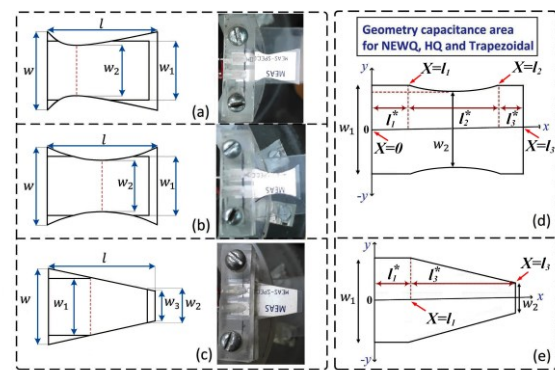

Fig. 2. Geometry of cantilevers (a) NEWQ sample, (b) HQ sample, (c) Trapezoidal, (d) Active layers for NEWQ and HQ and (e) active layers for Trapezoidal.

TABLE I
DIMENSIONS OF THE SAMPLES

	Beam Width (μm)				Beam length (μm)			
Sample	W	W_1	W_2	W_3	l	l_1^*	l_2^*	l_3^*
I	13000	10043	8290	–	16256	1142	8161	5722
II	13000	10043	8410	–	16256	3703	8644	2677
III	13000	10043	4835	4166	16256	5182	–	9843

The crystalline nature of PVDF and Ag are confirmed by XRD analysis as shown in Fig. 3. The peaks of the Brag's diffraction are found at 20.64° and 25.99° for PVDF and for Ag at 38.13 °,44.33° and 64.45° which corresponds to (110) and (022) for PVDF and for Ag (111), (200) and (220). The films are found to be monoclinic with lattice parameter for PVDF ($a = 4.97 \, Å$, $b = 9.67 \, Å$, $c = 9.24 \, Å$) and cubic for Ag ($a = b = c = 4.077 \, Å$).
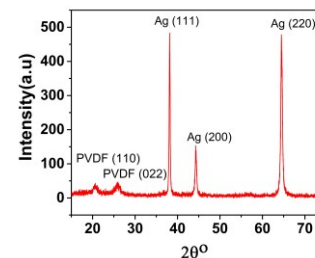

Fig. 3. X-ray diffraction pattern of the sample.

TABLE II
MECHANICAL AND ELECTRICAL PROPERTIES OF LAYERS OF THE SAMPLE

Material	Mechanical and electrical properties	
Polyvinylidene fluoride (PVDF)	Piezoelectric constant	$d_{31} = 23 \times 10^{-12} \text{C N}^{-1}$
	Relative Permittivity	$\varepsilon_r = 16$
	Young's modulus	$E_p = 2 - 4\text{GPa}$
	Poisson's ratio	$v_p = 0.35$
	Density	$\rho_p = 1780(\text{Kg/m}^3)$
Polyster (PET), Mylar	Young's modulus	$E_{PET} = 1.4\text{GPa}$
	Poisson's ratio	$v_{PET} = 0.4$
	Density	$\rho_{PET} = 930(\text{Kg/m}^3)$
Silver (Ag)	Young's modulus	$E_e = 69\text{GPa}$
	Poisson's ratio	$v_e = 0.37$
	Density	$\rho_e = 10500(\text{Kg/m}^3)$
Acrylic	Young's modulus	$E_e = 3.9\text{GPa}$
	Poisson's ratio	$v_e = 0.4$
	Density	$\rho_e = 1190(\text{Kg/m}^3)$

III. THEORY

The analytical model of the unimorph multilayer cantilever has been derived based on Euler-Bernoulli equation [17], [22–24] .The Heaviside function $H(x)$ is used for each section of piezoelectric layer where the length of the cantilever is considered along x-axis. Thereby, the governing equation of motion of the beam can be expressed as:

$$\frac{\partial^2}{\partial x^2}\left[EI(x)\frac{\partial^2 w_r(x,t)}{\partial x^2}\right] + c_s I(x)\frac{\partial^5 w_r(x,t)}{\partial x^4 \partial t} + c_a \frac{\partial w_r(x,t)}{\partial t}$$
$$+ m(x)\frac{\partial^2 w_r(x,t)}{\partial t^2} + \frac{\partial^2 w_r(x,t)}{\partial x^2}[\vartheta(x)v(t)[H(x) -$$
$$H(x-L)]] = -m(x)\frac{\partial^2 w_b(x,t)}{\partial t^2} - c_a \frac{\partial w_b(x,t)}{\partial t} \quad (1)$$

Where, $w_r(x,t)$ is the relative transverse displacement at a distance x from the fixed end. $EI(x)$ is the flexural stiffness, $I(x)$ is the cross-sectional area moment of inertia and $w_b(x,t)$ is the transverse base displacement. $v(t)$ is the voltage across piezoelectric patch and $\vartheta(x)$ is the electromechanical coupling of the piezoelectric material and substrate. c_s is the equivalent strain damping and c_a is the air damping coefficient. The top and bottom of the piezoelectric material are completely coated by electrodes, but the entire substrate area is not covered by the piezoelectric or electrode layers. So, $m(x) = b(x)\rho_{PET}t_{PET} + y(x)\rho_{e1}t_{e1} + y(x)\rho_{PVDF}t_{PVDF} + y(x)\rho_{e2}t_{e2} + b(x)\rho_{AC}t_{AC}$, where $m(x)$ is the mass per unit length of substrate; $\rho_{PET}, \rho_{e1}, \rho_{PVDF}, \rho_{e2}$ and ρ_{AC} are the densities; $t_{PET}, t_{e1}, t_{PVDF}, t_{e2}$ and t_{AC} are the thickness of the substrate, lower electrode, piezoelectric material, top electrode and protect the layer of acrylic, respectively. The width of the cantilever changes along the length. The variable beam width can be obtained as follows.

$$b_q(x) = 2w\left((2 + 2w - 4w_2)\left(\frac{x}{l}\right)^2 + (-3 - w + 4w_2)\frac{x}{l} + 1\right)$$

$$b_t(x) = 2w\left(1 + (w_3 - 1)\left(\frac{x}{l}\right)\right) \quad (2)$$

$$y_q(x) = 2w_1\left(\left(\frac{x}{l_1}\right) + (2 + 2w_2 - 4w_1)\left(\frac{x}{l_3 - l_1}\right)^2 + (-3 - w_2 + 4w_1)\left(\frac{x}{l_3 - l_1}\right) + \left(\frac{x}{l_3 - l_2}\right)\right)$$

$$y_t(x) = 2w_1\left(\left(\frac{x}{l_1}\right) + \left(1 + (w_2 - 1)\right)\left(\frac{x}{l_3 - l_1}\right)\right) \quad (3)$$

Where $b(x) = b_q(x) \text{ or } b_t(x)$ and $y(x) = y_q(x) \text{ or } y_t(x)$

The relative transverse displacement beam can be defined by an absolutely and uniformly convergent series of the eigenfunctions as

$$w_r(x,y) = \sum_1^\infty \eta_r(t)\phi_r(t) \quad (4)$$

Here, η_r is the unknown modal coordinate. The mass normalization $\phi_r(x)$ for infinite vibration modes of the cantilever can be obtained by the (5). λ_r is the dimensionless resonance frequency which is assumed for undamped free vibration system[25,26]

$$\phi_r(x) = \sqrt{\frac{1}{\int_0^l m(x)dx}}\left[\cosh\frac{\lambda_r}{l}x - \cos\frac{\lambda_r}{l}x - \sigma\left(\sinh\frac{\lambda_r}{l}x - \sin\frac{\lambda_r}{l}x\right)\right] \quad (5)$$

$$\sigma = \frac{\sinh\lambda_r - \sin\lambda_r}{\cosh\lambda_r + \cos\lambda_r}$$

The force function $f_r(t)$ can be obtained by summation of damping $f_r^c(t)$ and excitation function $f_r^m(t)$ at any position of length axis [24] as:

$$f_r^m(t) = -\left(\int_{x=0}^l m(x)\phi_r(x)dx \times \frac{d^2 g(t)}{dt^2} + \int_{x=0}^l xm(x)\phi_r(x)dx \times \frac{d^2 h(t)}{dt^2}\right) \quad (6)$$

$$f_r^c(t) = -c_a\left(\int_{x=0}^l \phi_r(x)dx \times \frac{dg(t)}{dt} + \int_{x=0}^l x\phi_r(x)dx \times \frac{dh(t)}{dt}\right) \quad (7)$$

$$f_r(t) = f_r^m(t) + f_r^c(t) \quad (8)$$

The transverse deflection response in each part of unimorph cantilever can be expressed as:

$$w_r(x,t)$$
$$= \sum_{i=0}^{\infty} \frac{\sqrt{\frac{1}{\int_0^l m(x)dx}} \left[\cosh\frac{\lambda_r}{l}x - \cos\frac{\lambda_r}{l}x - \sigma\left(\sinh\frac{\lambda_r}{l}x - \sin\frac{\lambda_r}{l}x\right)\right]}{\omega_{rd}}$$
$$\times \int_{\tau=0}^{t} f_r(\tau)e^{-\xi_r\omega_r(t-\tau)}\sin\omega_{rd}(t-\tau)d\tau \quad (9)$$

The mass normalized mode shapes which are used in the orthogonality conditions can be modified as[27][28]:

$$\int_0^L \phi_s(x)m(x)\phi_r(x)dx = \delta_{rs},$$
$$\int_0^L \phi_s(x)EI(x)\phi_r^{IV}(x)dx = \omega_r^2\delta_{rs} \quad (10)$$

The function of two variable can be defined by δ_{rs} or Kronecker delta. By substituting (4) into (1) and applying the orthogonality conditions as in (10) in the modal space, the equation of motion of the modal response with respect to the length of the beam can be estimated as

$$\frac{d^2\eta_r(t)}{dt^2} + 2\xi_r\omega_r\frac{d\eta_r(t)}{dt} + \omega_r^2\eta_r(t) + x_rv(t) = f_r(t) \quad (11)$$

Where x_r denotes backwards modal coupling as

$$x_r = \frac{d(\vartheta(x)\phi_r(x))}{dx}\bigg|_l = \vartheta(l)'\phi_r(l) + \vartheta(l)\phi_r'(l) \quad (12)$$

Duhamel integral in modal response can be obtained by making use of (11) as

$$\eta_r(t) = \frac{1}{\omega_r\sqrt{1-\xi_r^2}}\int_{\tau=0}^{t}[f_r(\tau)$$
$$-x_rv^*(\tau)]e^{-\xi_r\omega_r\sqrt{1-\xi_r^2}(t-\tau)}\sin\omega_r\left(\sqrt{1-\xi_r^2}\right)(t-\tau)d\tau \quad (13)$$

Where ω_r is the undamped natural frequency of the modes and ξ_r is the total damping ratio (strain rate damping and viscous air damping).

The voltage which is generated across the thickness (t_{PVDF}) of the piezoelectric material due to rearrangement of the electric field through Z axis is expressed as

$$v^*(t) = -E_3(t)t_{PVDF} \quad (14)$$

Due to the large thickness of the substrate, in comparison to the other layers, the position of the neutral axis can affect the stress/strain distribution across the PET material. The neutral axis position is shown in Fig. 4.

$\vartheta(x)$ is the electromechanical coupling of unimorph beam by considering the position of the top and bottom of the piezoelectric layer from the neutral axis of the beam

$$\vartheta(x) = -b(x)\frac{E_{PVDF}d_{31}}{2t_{PVDF}}(t_c^2 - t_b^2) \quad (15)$$
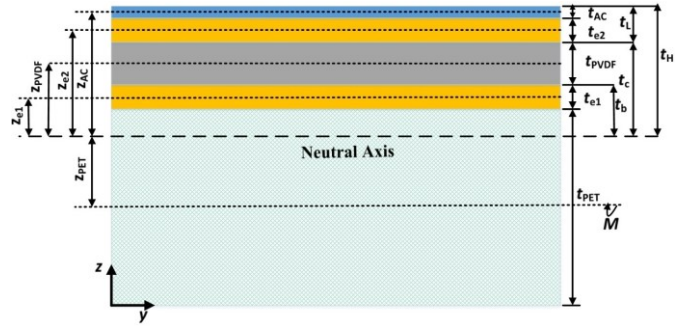$$t_c = t_H - t_L$$
$$t_b = t_H - (t_L + t_{PVDF}) \quad (16)$$

Fig. 4. The multilayer cantilever.

The effective moment of inertia for quadratic and linear shaped cantilever can be expressed as [29]

$$I(x) = b(x)\left(\frac{t_{PET}^3}{12} + t_{PET}z_{PET}^2\right) + y(x)\left(\frac{\eta_1^*,t_{e1}^3}{12} + t_{e1}z_{e1}^2\right)$$
$$+y(x)\left(\frac{\eta_2^*t_{PVDF}^3}{12} + t_{PVDF}z_{PVDF}^2\right) + y(x)\left(\frac{\eta_3^*t_{e2}^3}{12} + t_{e2}z_{e2}^2\right)$$
$$+b(x)\left(\frac{\eta_4^*t_{MY}^3}{12} + t_{AC}z_{AC}^2\right) \quad (17)$$

Where $\eta_1^*, \eta_2^*, \eta_3^*$ and η_4^* are the ratio of modulus of elasticity for four layers (lower electrode, piezoelectric layer, top electrode and protective layer) and substrate with $\eta_1^* = E_{e1}/E_{PET}$, $\eta_2^* = E_{PVDF}/E_{PET}$, $\eta_3^* = E_{e2}/E_{PET}$ and $\eta_4^* = E_{AC}/E_{PET}$. The total flexural rigidity, $EI(x)$, of the composite cantilever with variation of width along the length, can be expressed as

$$EI(x) = b(x)\left(\frac{t_{PET}^3}{12} + t_{PET}(z_{PET} - \bar{z})^2\right)$$
$$+ y(x)\left(\frac{t_{e1}^3}{12} + t_{e1}(z_{e1} - \bar{z})^2\right)$$
$$+ y(x)\left(\frac{t_{PVDF}^3}{12} + t_{PVDF}(z_{PVDF} - \bar{z})^2\right)$$
$$+ y(x)\left(\frac{t_{e1}^3}{12} + t_{e2}(z_{e2} - \bar{z})^2\right)$$
$$+ b(x)\left(\frac{t_{AC}^3}{12} + t_{AC}(z_{AC} - \bar{z})^2\right) \quad (18)$$

The normal stress ($\sigma_{PET}, \sigma_{e1}, \sigma_{PVDF}, \sigma_{e2}$ and σ_{AC}) of the multilayered beam is calculated by using constitutive piezoelectric equation

$$\sigma_{PET} = E_{PET}\varepsilon^{PET}(x,t)$$
$$\sigma_{e1} = E_{e1}\varepsilon^{e1}(x,t)$$
$$\sigma_{PVDF} = E_{PVDF}(\varepsilon^{PVDF}(x,t) - d_{31}E_3) \quad (19)$$
$$\sigma_{e2} = E_{e2}\varepsilon^{e2}(x,t)$$
$$\sigma_{AC} = E_{AC}\varepsilon^{AC}(x,t)$$

Where $E_{PET}, E_{e1}, E_{PVDF},$ and E_{AC} are the modulus of elasticity of the composite layers. The position of the neutral axis of the multilayer beam can be calculated by the following equation [30]

$$z = \frac{\begin{aligned}&((b(x).t_{PET}).\left(\frac{t_{PET}}{2} + t_{e1} + t_{PVDF} + t_{e2} + t_{AC}\right) + (y(x).\eta_1^*.t_{e1})\left(\frac{t_{e1}}{2} + t_{PVDF} + t_{e2} + t_{AC}\right) + \\ &(y(x).\eta_2^*.t_{PVDF})\left(\frac{t_{PVDF}}{2} + t_{e2} + t_{AC}\right) + (y(x).\eta_3^*.t_{e2})\left(\frac{t_{e2}}{2} + t_{AC}\right) + (b(x).\eta_4^*.t_{AC})\left(\frac{t_{AC}}{2}\right))\end{aligned}}{(b(x).t_{PET}) + (y(x).\eta_1^*.t_{e1}) + (y(x).\eta_2^*.t_{PVDF}) + (y(x).\eta_3^*.t_{e2}) + (b(x).\eta_4^*.t_{AC})} \tag{20}$$

M(x,t) is the moment of inertia along the cross-sectional beam in terms of change of the cantilever width:

$$M(x,t) = -\left(\int_{PET} \sigma_{PET} b(x)z dz \right.$$
$$+ \int_{e1} \sigma_{e1} b(x)z dz + \int_{PVDF} \sigma_{PVDF} b(x)z dz$$
$$\left. + \int_{e2} \sigma_{e2} b(x)z dz + \int_{AC} \sigma_{AC} b(x)z dz \right) \tag{21}$$

$$M(x,t) = EI(x)\frac{\partial^2 w_r(x,t)}{\partial x^2} - Kv^*[H(x) - H(x-L)]$$

The average strain on the plate for various layers in the cantilever material can be obtained for different geometries [31].

$$\varepsilon^*(x.t) = -z\frac{\partial^2 w(x,t)}{\partial x^2} \approx -\frac{M(x,t)z}{EI(x)} \tag{22}$$

A. Theory of charge and voltage distribution under deflection

The generated voltage across the electrodes is the integration of strain function distribution (22). Therefore, the increase in voltage depends on the increase of strain function [32].

$$V = -\frac{d_{31}E_{PVDF}t_{PVDF}}{c_{pQ}}\int_0^{l_3}\frac{M(x,t)z}{EI(x)}dx \tag{23}$$

where Q_i is the total charge generated by the piezoelectric material, which can be expressed by [33]

$$Q_i = -\int_0^{l_3} d_{31}E_{PVDF}t_{PVDF}\left(\frac{M(x,t)z}{EI(x)}\right)dx \tag{24}$$

The piezoelectric capacitance for NEWQ, HQ and Trapezoidal shapes may be obtained by (25).

$$c_i = \varepsilon_0 \varepsilon_{33}^T \frac{|Y_i|}{t_p} \tag{25}$$

The area of the truncated shape (samples I, II and III) can be estimated by (26) as follows. Where $w_1^* = w_1/2$, $w_2^* = w_2/2$ and $w^* = w/2$.

$$Y_Q = 2 \times [\int_0^{l_1} w_1^* dx + \int_{l_1}^{l_2} (w_1^*((2 + 2w_2^* - 4w_1^*)\left(\frac{x}{l}\right)^2$$
$$+ (-3 - w_2^* + 4w_1^*)\frac{x}{l} + 1))dx + \int_{l_2}^{l_3} w_1^* dx]$$

$$Y_T = 2 \times \left[\int_0^{l_1} w_1^* dx + \int_{l_1}^{l_3} w_1^*(1 + (w_2^* - 1)\frac{x}{l}dx\right] \tag{26}$$

Where $Y_i = Y_Q$ or Y_T and $C_i = C_Q$ or C_T

The corresponding output power can be expressed by the following equation

$$V_{o.c.i} = \frac{Q_i}{C_i} \; ; \; V_p = \left[\frac{V_{o.c.i}R_i}{2R_i}\right] = \frac{V_{o.c.i}}{2} \tag{27}$$

$$P_{out,i} = \left[\frac{V_{o.c.i}}{2R_i}\right]^2 \times R_i = \frac{(V_{o.c.i})^2}{(4R_i)} \; or \; \left(\frac{V_{o.c.i}}{R_L + R_i}\right)^2 \times R_i \tag{28}$$

Where V_p is the maximum amplitude. For a real load, the maximum power is transferred when R_i is equal to R_L.

$$|z_p| = \frac{1}{2\pi f_r.C_i} = R_L \tag{29}$$

Where, $V_{o.c.i}$ is the open circuit output voltage ($V_{o.c.i} \approx V$) and $P_{out,i}$ is the power across a discrete load resistance R_L, f_r is resonance frequency.

IV. SIMULATION USING FINITE ELEMENT METHOD

The Finite Element Method has been used to simulate the models and for comparison of the experimental measurements. The PC with Intel core i7 and 12Gb RAM has been used for the simulation. COMSOL Multiphysics is used to handle static and dynamic responses. The multilayer 3D models were developed based on FEM by applying mesh in models. Here, the triangular boundary for passive layer (sides of its edges) and mapping one for the middle of the geometry (active layers and passive in the middle one) has been considered (Fig. 5). To set the boundary condition, the cantilever has been fixed at the clamping edge in the solid mechanical interface. For electrostatic boundary conditions, the bottom of the piezoelectric layer (interface between electrode and PVDF) has been set as ground or zero potential and the top of PVDF is terminated to the external circuit along the piezoelectric layer. The charge on the peripheral surface of the beam is considered to be zero.
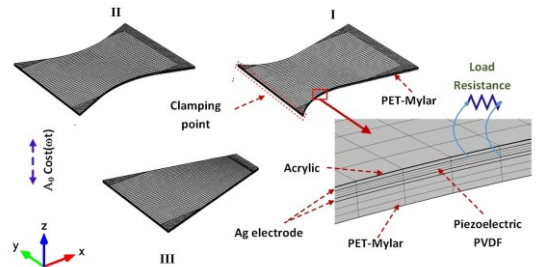

Fig. 5. Illustrated finite element model for Sample I, II and III.

The eigenfrequency analysis is essential to estimate the first resonance mode of the models. The static analysis under mechanical loading has been performed to evaluate the stress/strain distribution of the cantilevers. In addition, the frequency analysis based on harmonic excitation of the base is also carried out for a range of frequencies to calculate the approximate average power and output voltage generated by the

models.

The three designs of quadratic and linear-shaped structure has been studied for strain analysis by imposing a constant acceleration (0.1g). The contour graph in Fig. 6(a) shows the normalized strain distribution (NSD) on the top of PVDF/Ag. Zizys et al [34] claimed that the tensile and compression cause the change in strain distribution in Piezoeletric layer under sinusoidal vibration which occur at the same cycle of the period. Analysis shows that the generated strain distribution appears in the laminated part which is caused by the integrated effect of the piezoelectric layer and the electrode. The NEWQ produces more internal strain on the laminated part as compared to HQ and Trapezoidal shapes. Fig. 6(b) shows the strain distribution on the coverage area in each portion, the average is calculated according to the integration of all the 5000 bins laying on the laminated part. Here, the average strain distribution (ASD) on the relative area (percentage of values in each bin) of the surface of PVDF are negative values. The values, calculated for NEWQ, HQ and Trapezoidal are -1.40×10^{-7}, -1.26×10^{-7} and -1.00×10^{-7}, respectively. It is to be noted that the mass of the cantilever is the factor that provides more strain at near fixed clamped area. However, the strain reduces at the free end of the cantilever. In other words, from the center of the curve edge to the free end of the cantilever, the cantilever behaves as a flexible proof mass[35]. Due to the shape of the beam, mass per unit length effect is more on the free end of the beam, so the resonance frequency is reduced in NEWQ.
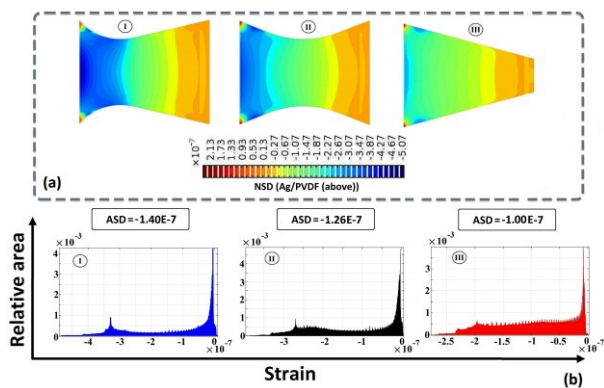

Fig. 6. The simulated result of three different samples (a) contour plot of the normalized strain distribution and (b) relative surface area versus strain distribution.

In a multilayer model like NEWQ strain transfers from outer layer (PET) to the inner PVDF material. The longitudinal strains of several layers in the form of a continuous function are shown in Fig. 7. The positive and negative strains are created unequally along the surface of each layer.

These strains cancel each other partly on the piezoelectric film which induces asymmetry charge on the surface of the film. It is noteworthy to mention that zero strain distribution is located at the natural axis position of the beam. If the designed substrate (PET) is very thin, then it will cause the neutral axis to lay inside of piezoelectric material. Due to this phenomena positive and negative charges will be produced inside the piezoelectric material. As the opposite charges cancels each

other hence less voltage will be generated. However, in a thick substrate, neutral axis lies out of the piezoelectric layer and as a result a net charge is created across the layer.
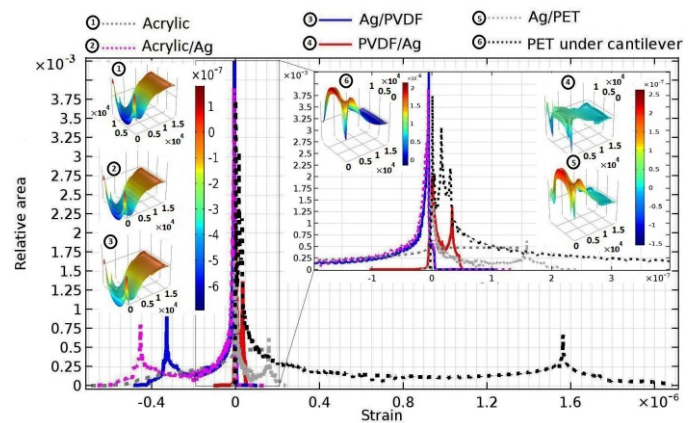

Fig. 7. The longitudinal strain in all parts of NEWQ considering the relative area in each portion.

The simulation results of the von Mises stress distribution of the first bending mode along the cantilevers are shown in Fig. 8. The result is stemmed from responses of the sample to 0.1g acceleration along z direction when beams are deformed in upwards direction. The maximum von Mises stress obtained for NEWQ, HQ and Trapezoidal are $4.32 \times 10^3 N/m^2$, $3.26 \times 10^3 N/m^2$ and $2.44 \times 10^3 N/m^2$, respectively. The maximum von Mises stress distribution is found to be more explicit at the fixed constant edge of all models which is highlighted with red colour. However, in NEWQ stress appears on the curve edge except the sides of the fixed clamped point.
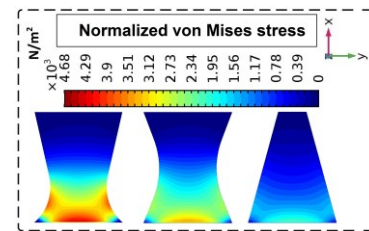

Fig. 8. Normalized von Mises stress of three different structures.

A. Simulation in Actuation

A numerical modeling of the piezoelectric actuator was conducted by applying FEM. Solid mechanical boundary conditions are applied in the FEM, as mentioned in the previous method. Although, in the electrostatics interface, bottom surface of PVDF is considered as the ground and the top of the piezoelectric layer has been taken as the electrode to apply the potential. Harmonic response analysis is carried out by using the parallel sparse direct solver and additionally, the nested dissection multithreaded preordering algorithm has been performed.

V. EXPERIMENTS

A vertical vibrator has been designed which functions as an external vibration source as shown in Fig.9.It is made from a loudspeaker (305 diameter and power 200/250 watt). The internal cone part is cut out and extracted from the basket of the loudspeaker to reduce the effect of the acoustic wave. Two pieces of rectangular epoxy glass beams are used to constrain the vibration along x and y. The amplitude and frequency of vibration can be adjusted and controlled by a signal generator and an audio power amplifier (FX-7000). The output voltage from PVDF samples is measured using an oscilloscope (Agilent DSO5052A). In order to measure the cantilever displacement, an optical arrangement has been setup. The samples are mounted on the center of the vibrator. A typical accelerometer (MMA7361) was attached to the same base to measure the acceleration created by the vibrator. Fig. 10 shows the accelerometer output for an acceleration of 1g (9.8m/s^2) which has a sensitivity of 800 mV/g.
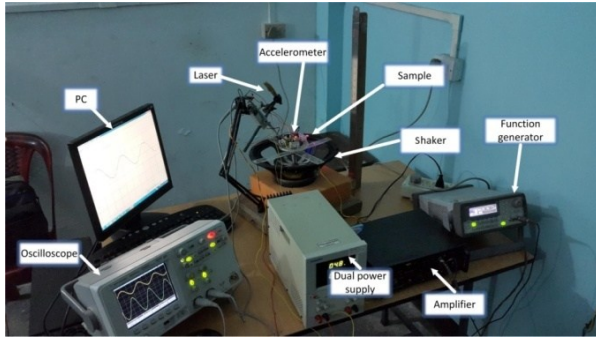

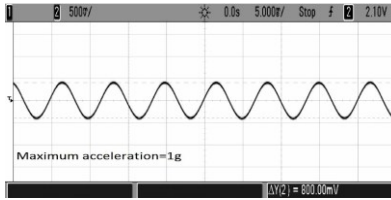Fig. 9. Experimental setup for the measurement prototype generator.

Fig. 10. Maximum acceleration used during the experiment.

For tip deflection measurement, an optical setup as shown in Fig. 11 has been arranged .The angle of bending is assumed to be zero at the equilibrium. The angle of incidence of the LASER beam at the tip of the un-deflected beam is α. When the tip vibrates the angle of incidence changes from γ to β. The displacement (L) of the reflected beam, as shown in the Fig. 11, is

$$L = L_1 - L_2 = \frac{L_3}{\tan \beta} - \frac{L_3}{\tan \gamma}. \tag{30}$$

The value of θ is expressed by[36]

$$\theta = \frac{\gamma - \alpha}{2} \ or \ \theta = \frac{-(\beta - \alpha)}{2} \tag{31}$$

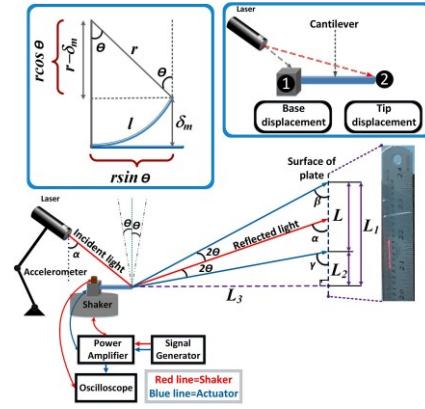The vertical tip displacement at the end of the beam can be derived for beam without proof mass as

Fig. 11. Measurement of tip displacement by using an optical setup.

$$\delta_n = r(1 - \cos \theta) = \frac{l(1 - \cos \theta)}{\sin \theta} \tag{32}$$

Where r is the radius of the beam bending.

Since $sin \theta = l/r$. When, $lim \theta \to 0$, $(\sin \theta) \approx \theta$. Then $\delta_n = l(1 - \cos \theta)/\theta$. This method is applied for actuation of the beam also. For this purpose, a sinusoidal voltage from an audio power amplifier is applied to the top and bottom of the PVDF NEWQ and tip displacement is measured.

VI. RESULTS

Fig. 12 shows the experimental results for the average power and the peak to peak voltage versus frequency for all the three
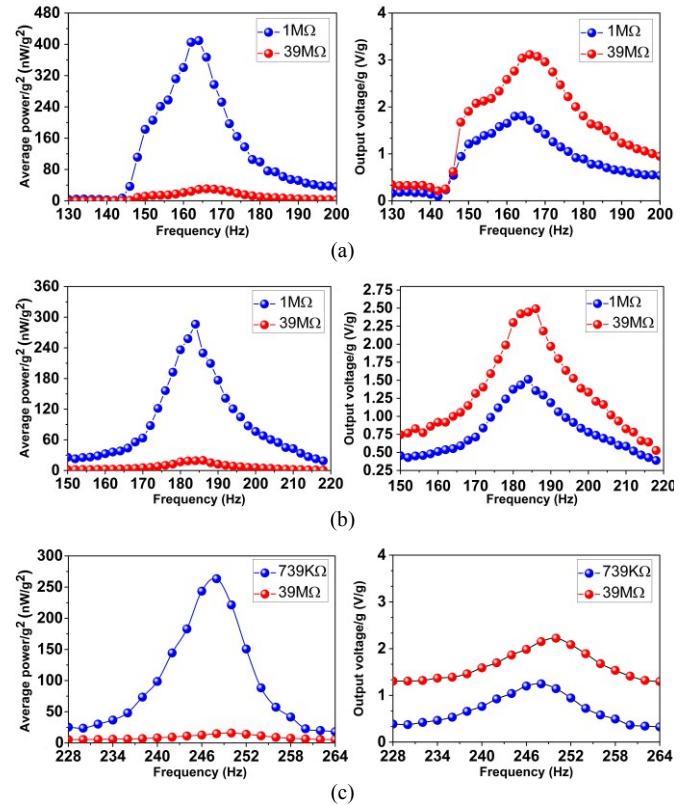

(a)

(b)

(c)

Fig. 12. The experimental results for each shape (a) NEWQ-sample I, (b) HQ-sample-II, (c) Trapezoidal sample-III.

samples. The blue line is the representation for the load resistance of $1M\Omega$ (matched load resistance) and the red line for the load resistance at $39M\Omega$. Fig. 12(a) represents the variation of NEWQ model, whereas Fig. 12(b) and (c) are for HQ and trapezoidal, respectively. As it is seen from Fig. 12(a) that NEWQ sample generates a voltage ($1.80Vg^{-1}$) and average power$409\,nWg^{-2}$ has been obtained at the optimal load resistance $1M\Omega$. The higher peak to peak voltage ($3.11Vg^{-1}$) as a function of frequency for $39M\Omega$ load has been obtained.Fig.12b are the results for the sample II (HQ) with an average power output of $286\,nWg^{-2}$ and maximum peak to peak voltage $1.51Vg^{-1}$ at load resistances of $1M\Omega$ and $39M\Omega$ respectively. Fig. 12(c) presents the variations for sample III (trapezoidal) in which the lowest average power ($263\,nWg^{-2}$) at optimum load resistance ($739K\Omega$) and the highest voltage ($1.24Vg^{-1}$) for $39M\Omega$.

Due to the effect of internal structure, air damping is different in the samples which causes loss of energy or damping. The quality factor is expressed by the half-power bandwidth method as [37]:

$$Q = \frac{f_r}{\Delta f} = \frac{f_r}{f_h - f_l} \qquad (33)$$

$$\xi = \frac{1}{2Q} \qquad (34)$$

f_r is the resonance frequency, f_h and f_l are two high and low -3dB frequencies.

Comparison of simulation and experimental results have been presented in Fig. 13. The samples have been excited at different acceleration levels ranging from $0.1g$ to $1g$ at various frequencies close to the resonance frequencies in order to compare the performance of the samples with different shapes. In all the samples, the variation of the average power/g² increases sharply until they approach the highest average power/g² at resonance frequency (NEWQ=164 Hz, HQ=184 Hz and Trapezoidal=248 Hz) then they start decreasing in the same manner. The numerical simulation result shows resemblance with the experimental one at the resonance frequency. When the cantilever beam is clamped in correct position, the resonant frequency is almost close to each other.
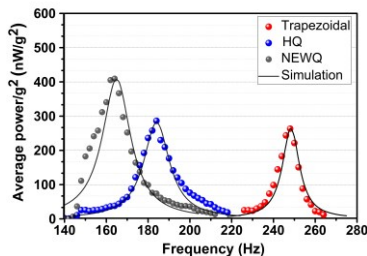

Fig. 13. Experimental and simulation results of maximum average power comparison for sample I-III.

The experimental and simulation curve deviates slightly in the case of the NEWQ model. This observed nonlinearity is due to the fact that the property of the PVDF changes under larger stress/strain distribution in multilayer stacks. Moreover, the piezoelectric constant in samples tend to increase in comparison to a linear model due to the increase in longitudinal strain in

piezoelectric patch [38].

In order to analyze the nonlinearity, coefficient of determination R^2 is calculated from experimental data as well as from the simulation models. The nonlinear curve fitting has been applied to all the three models, as well as their experimental data using Lorentz function. R^2 describes the non-linear relationships between the predictors and the response variables. The experimental data reveal the value of R^2 for different samples NEWQ, HQ and Trapezoidal as 0.96133, 0.98245 and 0.98508 respectively. The value of R^2 found from the models are 0.9992, 1 and 1 for the samples respectively. The coefficient of determination evaluated from experimental data is almost close to 1 in trapezoidal one, whereas the coefficient of determination value in the NEWQ sample is slightly lower than the HQ and trapezoidal sample. The difference between the coefficient of determination calculated from the experiment and simulation for NEWQ is a bit higher as compared to the other samples. In addition, due to increase in nonlinearity in the sample 'I' it shows better performance in frequency bandwidth (NEWQ$\cong$ 11.79Hz) than the others (HQ$\cong$ 9.92Hz and Trapezoidal$\cong$ 6.73Hz).

The FEM simulation results shown in Fig. 14 indicate that power output versus frequency of excitation across 15 different load impedances ranging from $44k\Omega$ to $4.74M\Omega$ for all the models: I, II and III. Evidently, the NEWQ harvester produces higher average power at the particular load resistance.
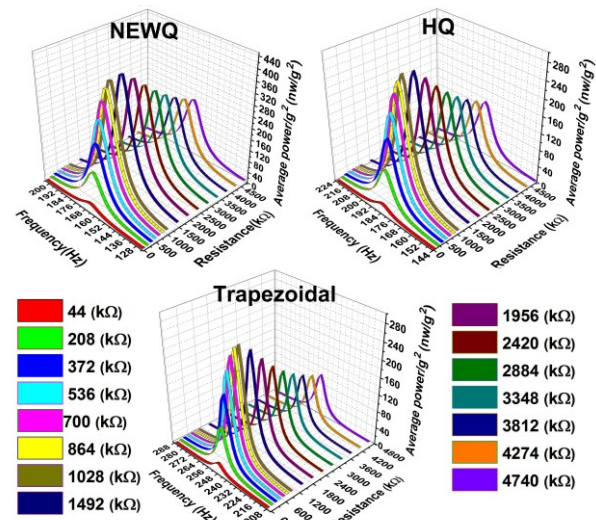

Fig. 14. The optimum power harvesting is obtained from models were coupled to various external load resistance and derived excitation frequency NEWQ, HQ and Trapezoidal (I, II and III).

It is possible to calculate the performance of models regarding developed average power in the NEWQ and HQ harvesters which are almost 54.9% and 8% more than that of trapezoidal harvester respectively. The variation of optimum power as a function of the excitation frequency for different quadratic shapes are shown in Fig. 15. In order to study the performance of energy harvesters the thickness to substrate

TABLE III
EXPERIMENTAL RESULTS OF SEVERAL SENSORS AS ENERGY HARVESTER

Type (—)	Material	Volume of device(mm^3)	Power ($nW.g^{-2}$)	Voltage p-p ($V.g^{-1}$)	Damp ξ	Quality factor ,Q	Frequency(Hz)	$R_L(\Omega)$	NPD ($nW.g^{-2}.Hz^{-1}.cm^{-3}$)
NEWQ[1]	PVDF	41.19	409.2	1.80	0.0604	8.2648	164	$1M\Omega$	60.54
HQ[1]	PVDF	41.17	285.2	1.51	0.0457	10.92	184	$1M\Omega$	37.62
Trapezoidal[1]	PVDF	34.8	262	1.24	0.022	22.72	248	$739k\Omega$	30.35
Rectangular [1]	PVDF	52.62	306	1.64	0.024	20.83	195	$1.1M\Omega$	29.81
Rectangular [2] [10]	ZnO	11.5	941	1.22	---	---	1300	$380k\Omega$	62.80
Rectangular [1] [9]	PZT	0.075	0.34	0.00027	0.0077	64.93	9275	$220k\Omega$	0.489
Trapezoidal [2] [11]	PZT	1.19	20.5	0.044	0.0001	415	232	$9k\Omega$	73.90

1 Without proof mass
2 With proof mass

ratio for a fixed resonances has been considered.

A cantilever of length l with width w at the curved edge has been considered in the simulation. During the simulation the width has been varied from the middle of the cantilever ($l/2$) to near to the fixed end ($l/10$) at five different positions of the beam. In the principal axis of the beam, the ratio of width to length is 1 at ($l/2$) and 0.2 at ($l/10$). Also, the ratio of thickness to substrate changes from 0.85 to 1. This is due to the influence of substrate's stiffness in resonance frequency.

In the simulation, the electrical load resistance is considered to be $1M\Omega$ and damping ratio as 3 percent. The results show that movement of curved edge towards fixed end of the cantilever has caused significant power enhancement in quadratic shape. The NEWQ cantilever with low width to length ratio (0.8) and highest thickness to substrate ratio (0.88) provides highest average power. It is obvious from (20) the neutral axis almost lies in optimized position, so, the maximum charge generation occurs on the piezoelectric layer.

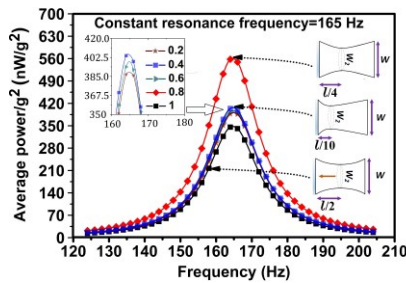The highest width to length ratio (1) with the thickness to

Fig. 15. Tapering with shifting shape from HQ to NEWQ by changing the thickness ratio.

substrate ratio (0.85) produces the lowest average power almost equal to 345nW/g^2 in HQ.

Fig. 16 shows the peak to peak voltage and average power obtained as a function of acceleration for the samples I to III when all beams were excited at first resonance frequency (164Hz, 184 Hz and 248Hz). If the internal resistance of PVDF piezoelectric is equal to the external load resistance, it will result in the highest average power extraction in the samples. When the optimal load resistance of $1M\Omega$, $1M\Omega$ and 739KΩ were coupled with pizoelectric materials, the voltages 1.80 V/g ,1.51V/g and 1.24V/g were measured in the sample I,II and III, the average powers of 409.2nW/g^2, 285nW/g^2 and 262nW/g^2 were delivered. As observed in NEWQ harvester, it generates much more power than conventional shape HQ and trapezoidal.

The simulated output power versus load resistance agrees well with the experimental results as shown in the figures. The sample II provided almost constant power stability in higher
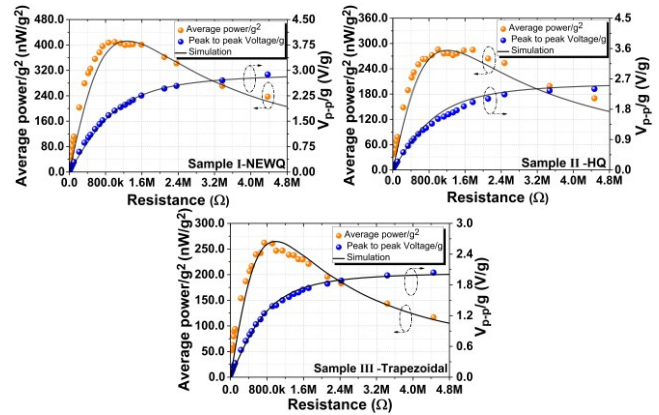

Fig. 16. The voltage peak to peak /power generated as a function of electrical load resistance for the sample I-III

load resistance R>1MΩ which seems to have a little disparity with the linear model.

The voltage and average power output of the rectangular sample as a function of resistive load are plotted in Fig. 17(a), where the excitation frequency of vibration is 195 Hz. The average power is found to be306 $nW\,g^{-2}$ at the optimal load resistance1.1$M\Omega$ for this sample and the result of peak to peak voltage is $1.64V\,g^{-1}$. The slight discrepancy between observed and simulated results may be due to the variations of the material properties, the PET thicknesses as well as capacitance value with considering the variation of dielectric material. The thickness variation of the PVDF material could be the main
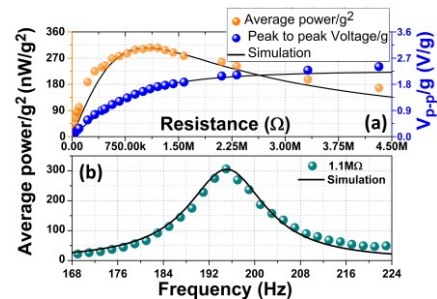

Fig. 17. (a) Simulation and experimental average power and peak to peak voltage values versus load resistance for the rectangular generator, (b) the average power versus the vibration frequency.

drawback between experiment and simulation results.

Fig. 17(b) exhibits the average power spectra as functions of vibration frequency when rectangular generator connected with 1.1 $M\Omega$ load resistance.

Table III provides a comparison of the samples I, II, III, rectangular and other published harvesters with different parameters. These parameters, obtained from the characterized data, are usually used to carry out metric comparison of different systems. The normalized power densities (NPD) were calculated taking into consideration the effective volume of the selected samples. The piezoelectric polymers typically generate low power output as compared to ceramic-based piezoelectric. However, the shape optimization helps to improve NPD. NPD of sample NEWQ, which is almost comparable with the PVEH types which are reported in the literatures [10] and [11]. It was found that the optimum design reported in this work has a lowest resonance frequency (164 Hz) without proof mass. It is obtained the highest NPD in PVEH within the suitable resonance frequency (<200Hz).

The output power of NEWQ device was better than other samples as well as PZT based as a rectangular harvester and trapezoidal harvester with seismic mass demonstrated by other reports [9,11]. The disadvantage of these devices is the optimum load resistance greater than other works [9-11]. This may be due to the low electromechanical coupling coefficient of PVDF film.

Fig. 18 shows the calculation of NPD for other quadrilateral traditional sample (rectangular) making use of the present experimental method. Traditional shapes such as rectangular shape show the lowest NPD 29.82 $(nW.g^{-2}.Hz^{-1}.cm^{-3})$. However, the approximate NPD for the proposed novel NEWQ was 60.54 $(nW.g^{-2}.Hz^{-1}.cm^{-3})$, signifying its favourability among the rest of the three samples.
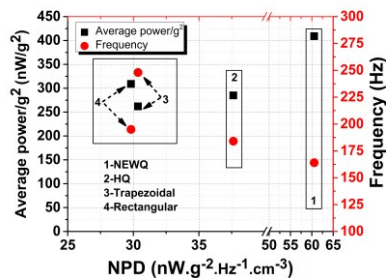

Fig. 18. Average power and natural frequency for four different samples versus the NPD (Normalized power density).

The frequency range of 134 Hz to 196 Hz with an interval of 4 Hz was applied to the unimorph NEWQ sample (Fig. 19(a)). The tip displacement was measured at an acceleration of 0.185g by making use of the developed optical setup. The tip displacement and relative displacement were measured and calculated at an acceleration of 0.185 g by making use of the developed optical setup. The amplitude of base displacement is small as compared to the tip displacement. So, we used a piece of polished Si (mirror) at the top of the base for observing the reflection in long distance between sample and surface plates. The difference between the base displacement and tip displacement is 56.8 μm at the peak. The displacement of base

at 0.185 g is low as compared to tip displacement which can be negligible. The AC excitation voltage of 74V was applied to the top and bottom surface of PVDF layer for measure tip displacement. In order to compare maximum tip displacement over excitation frequency, FEM simulation were conducted for both the cases (vibrator and actuator). One can see that the FEM result agrees well with the theoretical calculation (32) in both actuation and energy harvesting application. It is observed that air damping can significantly affect the prototype for actuation and vibration operation. This provides more nonlinearity in deflection when input acceleration is applied to the sample.

Fig. 19(b) illustrates the measurement of acceleration versus output power. The cantilever (NEWQ) was set at a range of input acceleration of 0.25g to 1g and the load resistance is $R = 1M\Omega$. As it is clear from this figure, the output power has increased dramatically which is fitted with a nonlinear curve. The maximum amount of power has been obtained in NEWQ. The stiffness of the cantilever and damping ratio are the two most important parameters which effect the nonlinearity in response of piezoelectric material [39].
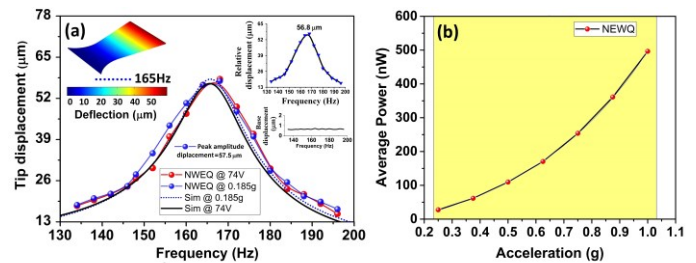

Fig. 19. (a) NEWQ based on acceleration and actuation and (b) Maximum power as a function of acceleration obtained by accelerometer.

Fig. 20(a) illustrates the simulated histogram as well as contour of strain distribution analysis for several models. The models named as types A, A', A'', B, B', C and C'. Models A, B and C are equal in volume (approximate volume of trapezoidal without proof mass). Models B' (i.e. attached with a proof mass of 10.23 mg with approximate total volume of 35.95 mm^3 and resonance frequency of 184.9 Hz) and C' (i.e. attached with a proof mass of 5.11 mg with approximate total volume of 35.37 mm^3 and frequency 159.2 Hz) are compared with models A (at 146.4Hz) and the reduction of size in same models (A' and A'' with approximate total volume 29.2 mm^3 and 27.4 mm^3 and resonance frequencies of 131.8 Hz and 125Hz, respectively). The ASD are calculated in models A, B' and C' with-1.51×10^{-7} ,-1.49×10^{-7} and -1.49×10^{-7}respectively. The ASD is more for models A' (-1.61×10^{-7}) and A''(-1.69×10^{-7}) as compared the other rest of the models. Fig. 20(b) extended the study without changing the traditional rectangular model (without and with proof mass A and B' (total volume 53.37 mm^3 with 10.23 mg proof mass and resonance frequencies of 163 Hz)). It is also observed that the ASD for model B' (with proof mass) is equal to the model A'' (NEWQ) without proof mass.
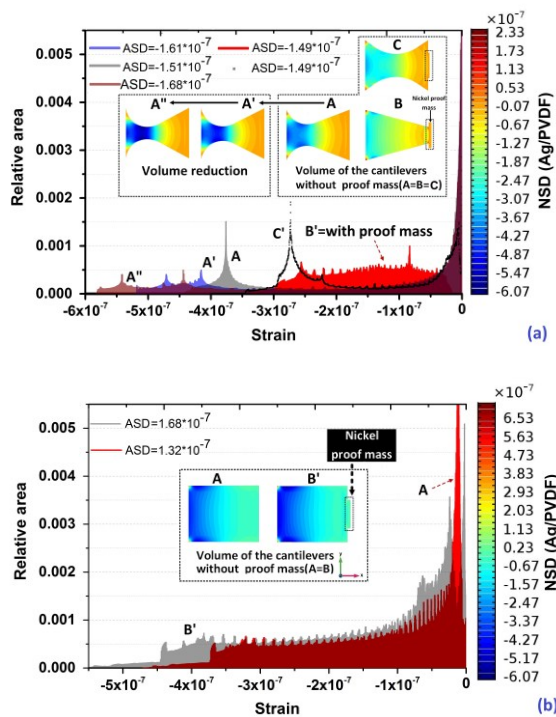
Fig. 20. (a) Optimum configuration of models and (b) Conventional models of PVEH (with and without seismic mass).

VII. CONCLUSION

In this work, the piezoelectric film (PVDF) sample with truncated shapes without attaching the poof mass at the free end was optimized, designed and characterized. The model was investigated based on Euler–Bernoulli beam theory where the beams were subjected to vertical excitation. The previous studies by the authors was concentrated on a traditional model without proof mass [40], [24]. Here it is tried to investigate three different types of beam geometry NEWQ, HQ and Trapezoidal. The proposed model of NEWQ performs significantly better and power extraction shows improvement in unimorph cantilever. The NEWQ sample shows higher power ($409.2\ nW.g^{-2}$) and normalized power density ($60.54\ nW.g^{-2}.Hz^{-1}.cm^{-3}$) in NEWQ than HQ and trapezoidal shapes. According to the results, resonance frequency has been shifted for different shapes. FEM simulation reveals that influence of mass per unit area can lead to a high longitudinal strain near the clamped area of the cantilevers. The strain distribution over the relative surface area has been found to be higher in NEWQ, compared to HQ and trapezoidal cantilever, but strain distribution over the relative surface area is uniform in trapezoidal cantilever. It is observed that when the near edge of the cantilever moves towards the anchor, while considering thickness and length ratio the average power tends to increase at constant resonance frequency. Additionally, the strain distribution changes in each layer. NEQW model (without proof mass) with a minimum width at curved edge provides equal ASD with conventional model with nickel proof mass at free end. This may result in size reduction for future mobile devices, wireless sensor network modules.

Due to the absence of the proof mass the volume of the harvester will decrease.

REFERENCES

[1] J. Granstrom, J. Feenstra, H. A. Sodano, and K. Farinholt, "Energy harvesting from a backpack instrumented with piezoelectric shoulder straps," *Smart Mater. Struct.*, vol. 16, no. 5, pp. 1810–1820, Oct. 2007.

[2] A. Delnavaz and J. Voix, "Piezo-earpiece for micro-power generation from ear canal dynamic motion," *J. Micromechanics Microengineering*, vol. 23, no. 11, p. 114001, Nov. 2013.

[3] S. Yu, W. Zheng, W. Yu, Y. Zhang, Q. Jiang, and Z. Zhao, "Formation mechanism of β-phase in PVDF/CNT composite prepared by the sonication method," *Macromolecules*, vol. 42, no. 22, pp. 8870–8874, Nov. 2009.

[4] M. E. Achaby, F. Z. Arrakhiz, S. Vaudreuil, E. M. Essassi, and A. Qaiss, "Piezoelectric β-polymorph formation and properties enhancement in graphene oxide – PVDF nanocomposite films," *Appl. Surf. Sci.*, vol. 258, no. 19, pp. 7668–7677, Jul. 2012.

[5] I. Patel, E. Siores, and T. Shah, "Utilisation of smart polymers and ceramic based piezoelectric materials for scavenging wasted energy," *Sensors Actuators A Phys.*, vol. 159, no. 2, pp. 213–218, May 2010.

[6] B. Gusarov, "PVDF piezoelectric polymers : characterization and application to thermal energy harvesting," Nov. 2015.

[7] N. S. Shenck and J. A. Paradiso, "Energy scavenging with shoe-mounted piezoelectrics," *IEEE Micro*, vol. 21, no. 3, pp. 30–42, May 2001.

[8] D. Vatansever, R. L. Hadimani, T. Shah, and E. Siores, "Voltage response of piezoelectric PVDF films in vacuum and at elevated temperatures," *Smart Mater. Struct.*, vol. 21, no. 8, p. 85028, Aug. 2012.

[9] D. Isarakorn, D. Briand, P. Janphuang, A. Sambri, S. Gariglio, J.-M. Triscone, F. Guy, J. W. Reiner, C. H. Ahn, and N. F. de Rooij, "The realization and performance of vibration energy harvesting MEMS devices based on an epitaxial piezoelectric thin film," *Smart Mater. Struct.*, vol. 20, no. 2, p. 25015, Feb. 2011.

[10] P. Wang and H. Du, "ZnO thin film piezoelectric MEMS vibration energy harvesters with two piezoelectric elements for higher output performance," *Rev. Sci. Instrum.*, vol. 86, no. 7, p. 75002, Jul. 2015.

[11] L. M. Miller, E. Halvorsen, T. Dong, and P. K. Wright, "Modeling and experimental verification of low-frequency MEMS energy harvesting from ambient vibrations," *J. Micromechanics Microengineering*, vol. 21, no. 4, p. 45029, Apr. 2011.

[12] B. Montazer and U. Sarma, "Modeling and analysis the effect of PZT area on square shaped substrate for power enhancement in MEMS piezoelectric energy harvester," *J. Circuits, Syst. Comput.*, vol. 26, no. 9, p. 1750128, Sep. 2017.

[13] S. Saxena, R. Sharma, and B. D. Pant, "Design and development of guided four beam cantilever type MEMS based piezoelectric energy harvester," *Microsyst. Technol.*, vol. 23, no. 6, pp. 1751–1759, Jun. 2017.

[14] Z. Yang, Y. Q. Wang, L. Zuo, and J. Zu, "Introducing arc-shaped piezoelectric elements into energy harvesters," *Energy Convers. Manag.*, vol. 148, pp. 260–266, Sep. 2017.

[15] J. Park, S. Lee, and B. M. Kwak, "Design optimization of piezoelectric energy harvester subject to tip excitation," *J. Mech. Sci. Technol.*, vol. 26, no. 1, pp. 137–143, Jan. 2012.

[16] S. Ben Ayed, A. Abdelkefi, F. Najar, and M. R. Hajj, "Design and

This article has been accepted for publication in a future issue of this journal, but has not been fully edited. Content may change prior to final publication. Citation information: DOI 10.1109/JSEN.2018.2818822, IEEE Sensors Journal

12

performance of variable-shaped piezoelectric energy harvesters," *J. Intell. Mater. Syst. Struct.*, vol. 25, no. 2, pp. 174–186, Jan. 2014.

[17] H. Salmani, G. H. Rahimi, and S. A. Hosseini Kordkheili, "An exact analytical solution to exponentially tapered piezoelectric energy harvester," *Shock Vib.*, vol. 2015, pp. 1–13, Jul. 2015.

[18] J. Lee and B. Choi, "A study on the piezoelectric energy conversion system using motor vibration," *Int. J. Precis. Eng. Manuf.*, vol. 13, no. 4, pp. 573–579, Apr. 2012.

[19] N. A. Siddiqui, D.-J. Kim, R. A. Overfelt, and B. C. Prorok, "Electromechanical coupling effects in tapered piezoelectric bimorphs for vibration energy harvesting," *Microsyst. Technol.*, vol. 23, no. 5, pp. 1537–1551, May 2017.

[20] M. I. Friswell and S. Adhikari, "Sensor shape design for piezoelectric cantilever beams to harvest vibration energy," *J. Appl. Phys.*, vol. 108, no. 1, p. 14901, Jul. 2010.

[21] C. K. Thein and J.-S. Liu, "Numerical modeling of shape and topology optimisation of a piezoelectric cantilever beam in an energy-harvesting sensor," *Eng. Comput.*, vol. 33, no. 1, pp. 137–148, Jan. 2017.

[22] A. Erturk, "Electromechanical modeling of piezoelectric energy harvesters," *Heal. San Fr.*, 2009.

[23] X. Gao, W.-H. Shih, and W. Y. Shih, "Vibration energy harvesting using piezoelectric unimorph cantilevers with unequal piezoelectric and nonpiezoelectric lengths.," *Appl. Phys. Lett.*, vol. 97, no. 23, p. 233503, Dec. 2010.

[24] A. Erturk and D. J. Inman, "A distributed parameter electromechanical model for cantilevered piezoelectric energy harvesters," *J. Vib. Acoust.*, vol. 130, no. 4, p. 41002, Aug. 2008.

[25] S. Peng, X. Zheng, J. Sun, Y. Zhang, L. Zhou, J. Zhao, S. Deng, M. Cao, W. Xiong, and K. Peng, "Modeling of a micro-cantilevered piezo-actuator considering the buffer layer and electrodes," *J. Micromechanics Microengineering*, vol. 22, no. 6, p. 65005, Jun. 2012.

[26] A. Jemai, F. Najar, and M. Chafra, "Parametric analysis of multilayered unimorph piezoelectric vibration energy harvesters," *J. Vib. Control*, vol. 23, no. 15, pp. 2538–2553, Aug. 2017.

[27] A. Erturk and D. J. Inman, *Piezoelectric energy harvesting*. Wiley, 2011.

[28] A. Erturk, O. Bilgen, and D. J. Inman, "Performance analysis of single crystal PMN-PZT unimorphs for piezoelectric energy harvesting," in *Smart Materials, Adaptive Structures and Intelligent Systems, Volume 1*, 2008, pp. 461–471.

[29] T. M. Kamel, R. Elfrink, M. Renaud, D. Hohlfeld, M. Goedbloed, C. de Nooijer, M. Jambunathan, and R. van Schaijk, "Modeling and characterization of MEMS-based piezoelectric harvesting devices," *J. Micromechanics Microengineering*, vol. 20, no. 10, p. 105023, Oct. 2010.

[30] C. T. Pan, Z. H. Liu, and Y. C. Chen, "Study of broad bandwidth vibrational energy harvesting system with optimum thickness of PET substrate," *Curr. Appl. Phys.*, vol. 12, no. 3, pp. 684–696, May 2012.

[31] B. L. Ooi, J. M. Gilbert, and A. R. A. Aziz, "Analytical and finite-element study of optimal strain distribution in various beam shapes for energy harvesting applications," *Acta Mech. Sin.*, vol. 32, no. 4, pp. 670–683, Aug. 2016.

[32] A. Čeponis, D. Mažeika, and V. Bakanauskas, "Trapezoidal cantilevers with irregular cross-sections for energy harvesting systems," *Appl. Sci.*, vol. 7, no. 2, p. 134, Jan. 2017.

[33] C. Dung and E. Sasaki, "Numerical simulation of output response of PVDF sensor attached on a cantilever beam subjected to impact loading," *Sensors*, vol. 16, no. 5, p. 601, Apr. 2016.

[34] D. Zizys, R. Gaidys, R. Dauksevicius, V. Ostasevicius, and V. Daniulaitis, "Segmentation of a vibro-shock cantilever-type piezoelectric energy harvester operating in higher transverse vibration modes," *Sensors*, vol. 16, no. 1, p. 11, Dec. 2015.

[35] M. Kim, S. Hong, D. J. Miller, J. Dugundji, and B. L. Wardle, "Size effect of flexible proof mass on the mechanical behavior of micron-scale cantilevers for energy harvesting applications," *Appl. Phys. Lett.*, vol. 99, no. 24, p. 243506, Dec. 2011.

[36] H. Liu, C. J. Tay, C. Quan, T. Kobayashi, and C. Lee, "Piezoelectric MEMS energy harvester for low-frequency vibrations with wideband operation range and steadily increased output power," *J. Microelectromechanical Syst.*, vol. 20, no. 5, pp. 1131–1142, Oct. 2011.

[37] B. A. Olmos and J. M. Roesset, "Evaluation of the half-power

bandwidth method to estimate damping in systems without real modes," *Earthq. Eng. Struct. Dyn.*, vol. 39, no. 14, pp. 1671–1686, Nov. 2010.

[38] A. Esmaeili and J. M. M. Sousa, "Power density ratio optimization of bimorph piezocomposite energy harvesters using a multidisciplinary design feasible method," *Compos. Struct.*, vol. 165, pp. 171–179, Apr. 2017.

[39] B. Yang, "Hybrid energy harvester based on piezoelectric and electromagnetic mechanisms," *J. Micro/Nanolithography, MEMS, MOEMS*, vol. 9, no. 2, p. 23002, Apr. 2010.

[40] S. Nabavi and L. Zhang, "Design and optimization of piezoelectric MEMS vibration energy harvesters based on genetic algorithm," *IEEE Sens. J.*, vol. 17, no. 22, pp. 7372–7382, Nov. 2017.

Babak Montazer. received M.Sc. degrees in electronics from the University of Pune, Pune, in 2011. He is currently pursuing the Ph.D. degree in the Department of Instrumentation & USIC at Gauhati University, Guwahati. His current research interests include investigation and characterization of piezoelectric MEMS transducers for energy harvesting device.

Utpal Sarma (M'14) received the M.Sc. degree in Physics and the Ph.D. degree from Gauhati University, Guwahati, India, in 1998 and 2010, respectively. In 1999, he joined the Department of Physics, B. Borooah College, Guwahati, as a Lecturer. He joined Gauhati University, as an Assistant Professor, in 2007, where he is currently a Professor. His current research interests include embedded system for agro industries, sensor instrumentation, and microenergy harvesting devices.